RESEARCH ARTICLE

National Science Review
7: 1879–1885, 2020
doi: 10.1093/nsr/nwaa163
Advance access publication 15 July 2020

[1]International Center for Quantum Materials, School of Physics, Peking University, Beijing 100871, China; [2]Department of Applied Physics, The Hong Kong Polytechnic University, Hong Kong, China; [3]Department of Physics, Pennsylvania State University, University Park, PA 16802, USA; [4]Department of Materials Science and Engineering, School of New Energy and Materials, China University of Petroleum, Beijing 102249, China; [5]Department of Materials Science and Engineering, University of Tennessee, Knoxville, TN 37996, USA; [6]Materials Science and Technology Division, Oak Ridge National Laboratory, Oak Ridge, TN 37831, USA; [7]Center for Advanced Quantum Studies, Department of Physics, Beijing Normal University, Beijing 100875, China; [8]CAS Center for Excellence in Topological Quantum Computation, University of Chinese Academy of Sciences, Beijing 100190, China; [9]Beijing Academy of Quantum Information Sciences, Beijing 100193, China and [10]Collaborative Innovation Center of Quantum Matter, Beijing 100871, China

*Corresponding authors. E-mails: jianwangphysics@pku.edu.cn; xcxie@pku.edu.cn
†Equally contributed to this work.

Received 18 December 2019; **Revised** 15 May 2020; **Accepted** 8 July 2020

PHYSICS

Unconventional Hall effect induced by Berry curvature

Jun Ge[1,†], Da Ma[1,†], Yanzhao Liu[1], Huichao Wang[1,2], Yanan Li[1,3], Jiawei Luo[1], Tianchuang Luo[1], Ying Xing[1,4], Jiaqiang Yan[5,6], David Mandrus[5,6], Haiwen Liu[7], X.C. Xie[1,8,9,10,*] and Jian Wang[1,8,9,10,*]

ABSTRACT

Berry phase and Berry curvature play a key role in the development of topology in physics and do contribute to the transport properties in solid state systems. In this paper, we report the finding of novel nonzero Hall effect in topological material $ZrTe_5$ flakes when the in-plane magnetic field is parallel and perpendicular to the current. Surprisingly, both symmetric and antisymmetric components with respect to magnetic field are detected in the in-plane Hall resistivity. Further theoretical analysis suggests that the magnetotransport properties originate from the anomalous velocity induced by Berry curvature in a tilted Weyl semimetal. Our work not only enriches the Hall family but also provides new insights into the Berry phase effect in topological materials.

Keywords: Berry curvature, topological material, Hall effect, tilted Weyl semimetal, Berry phase effect

INTRODUCTION

The concept of Berry phase was first proposed in 1984 and has led to significant breakthroughs in physical science [1]. In recent years, Berry curvature, first discussed in the one band effective dynamics of a Bloch electron [2,3], has become an important concept in condensed matter physics [4–13]. Numerous experimental investigations show that it has to be considered in the semiclassical electronic theory as a basic ingredient. Many interesting physical phenomena can be generated by Berry curvature, such as the intrinsic anomalous Hall effect [14–18], negative magnetoresistance (MR) [19,20] and nonlinear Hall effect [21,22]. In time-reversal symmetry broken or space-inversion symmetry broken systems, the nonzero Berry curvature can generate an anomalous velocity that is transverse to the applied electric field and thus gives rise to anomalous transport currents, making an intrinsic contribution to Hall conductivity [2,4]. Besides, Berry curvature can also affect the density of states in the phase-space, which leads to the violation of Liouville's theorem for the conservation of phase-space volume [23]. As a consequence, a correction term to the density of states dependent on magnetic field and Berry curvature is generated, which has profound effects on transport properties.

The emergence of Weyl semimetal provides a new platform to explore Berry curvature. Weyl semimetals host gapless bulk excitations described by Weyl equation and metallic Fermi arc states on the surface. As a result of band crossing between a pair of spin-non-degenerate bands, a Weyl node behaves like a magnetic monopole in momentum space and can generate divergent Berry curvature around the Weyl points [24–26]. The Berry curvature integrating over the Fermi surface enclosing a Weyl point gives a quantized topological charge, which equals the chirality of Weyl node [27]. Many interesting Berry curvature-related physical phenomena are proposed in Weyl semimetals, e.g. chiral anomaly [27,28]. Recently, it was proposed that the Berry curvature can give rise to a new type of planar Hall effect (PHE) in Weyl semimetals [29,30]. The proposed PHE appears when the electric and magnetic field are coplanar, symmetric with the magnetic field, and satisfies the angular relation: $\sigma_{yx}^{ph} = \Delta\sigma \sin\theta \cos\theta$, with θ denoting the angle between the electric and magnetic fields. When coplanar electric and magnetic field are aligned in parallel and perpendicular directions, the proposed PHE signal will

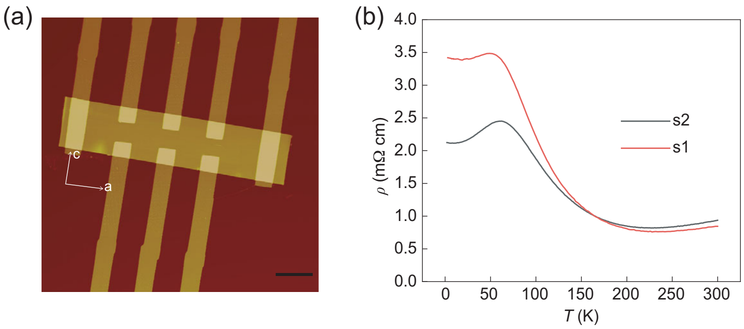

Figure 1. AFM image and ρ(T) behavior of $ZrTe_5$ devices. (a) AFM image of a typical $ZrTe_5$ device. The scale bar represents 10 μm. (b) Resistivity of $ZrTe_5$ devices (s1: 300 nm thick; s2: 225 nm thick) as a function of temperature from 300 K to 2 K. A resistivity peak is detected.

vanish. The systematic experimental studies on the relation between the PHE and the magnetic field, especially on the symmetric and antisymmetric properties and the angular dependence, are still highly desired.

In this work, we present the first experimental observation of nonzero Hall effect when the in-plane magnetic field is parallel and perpendicular to the current, which is clearly revealed by systematic and reliable magnetotransport studies in topological material $ZrTe_5$ devices. Specifically, when the magnetic field lies in *ac* plane of $ZrTe_5$ flakes, both symmetric and antisymmetric components are observed in Hall resistivity, which cannot be explained by previous consideration of the PHE. When the in-plane magnetic field is along *a* axis ($B \parallel I$) and *c* axis ($B \perp I$), nonzero in-plane Hall resistivity is detected after excluding extrinsic contributions from longitudinal MR caused by slight misalignment of electrodes and inevitable projection of normal Hall resistivity at *b* axis. This feature is also beyond the current theoretical understanding and experimental reports on the PHE, for which the Hall signal is zero when the coplanar magnetic field and current are parallel and perpendicular [29–34]. Our theoretical analysis reveals that the tilt term in Weyl semimetal gives rise to extra contribution to the Berry curvature-induced anomalous velocity, which can explain both the symmetric and antisymmetric properties and the angular dependence of Hall signals in our measurements. Thus, our findings reveal the new properties induced by Berry curvature.

RESULTS

$ZrTe_5$ is a layered material, with two-dimensional sheets in *ac* plane stacking along the *b* axis, and the interlayer van der Waals coupling strength is similar to that of graphite [35]. Flat $ZrTe_5$ flakes can thus easily be obtained by mechanical exfoliation. Many experimental investigations have indicated that $ZrTe_5$ can be a three-dimensional Dirac semimetal [36–39] depending on the unit cell volume of the specific crystals, and lots of interesting phenomena induced by nontrivial Berry curvature have been observed in $ZrTe_5$, such as chiral magnetic effect [36], recently reported PHE [31] and anomalous Hall effect [40]. In this work, $ZrTe_5$ flakes supported by 300 nm-thick SiO_2/Si substrates were mechanically exfoliated from high quality single crystals [38]. The standard e-beam lithography followed by e-beam evaporation was used to fabricate electrodes. Figure 1(a) shows the atomic force microscope (AFM) image of a typical device for electrical transport measurements. The crystal orientation is indicated by the white arrows. $ZrTe_5$ flakes are often narrow in the *c* axis as they are easily peeled off along *a* axis. Refined Hall structure configuration is used to detect Hall signals of $ZrTe_5$ devices on *ac* plane. Electric current is always along *a* axis and homogeneously goes through the device as current electrodes (I_+ and I_-) cover the whole flake. The typical longitudinal resistivity as a function of temperature from 300 K to 2 K is shown in Fig. 1(b). Device 1 (s1, 300 nm thick) and device 2 (s2, 225 nm thick) are selected as representatives here. With temperature decreasing from 300 K to 2 K, a resistivity peak can be clearly observed in both devices. This resistivity vs. temperature (ρT) behavior is different from the resistivity saturation at low temperatures for the bulk single crystals [38], from which the flakes are exfoliated. Another feature shown in ρT behavior is that the thinner flake exhibits higher temperature of the resistivity peak, which indicates the enhancement of the metallic state in thinner flakes. Previous studies show that this may be a consequence of the energy bands shifting [41].

We further explore the magnetotransport properties of $ZrTe_5$ flakes in the measurement configuration when magnetic field is aligned in *ac* plane. Figure 2(a) shows the schematic view of the angular-dependent magnetotransport measurement configuration. The magnetic field lies in *ac* plane and forms an angle θ relative to the electric current. Magnetic field is along *a* axis for $\theta = 0^\circ$ ($B \parallel I$) and along *c* axis for $\theta = 90^\circ (B \perp I)$. Figure 2(b) exhibits the longitudinal magnetoresistance (LMR) at selected angles taken in s2. Negative LMR is most evident at *a* axis ($B \parallel I$), which is consistent with the prediction of chiral anomaly. Moreover, negative LMR is detected in a large regime of about $\pm 20^\circ$, several times larger than that reported in bulk $ZrTe_5$ [36,40]. It may be due to the more precise angle control for $ZrTe_5$ thin flakes. Figure 2(c) shows the in-plane Hall resistivity after excluding the contribution from LMR caused by slight misalignment of electrodes, and the formula of the renormalized Hall resistivity reads $\rho_{yx}=$

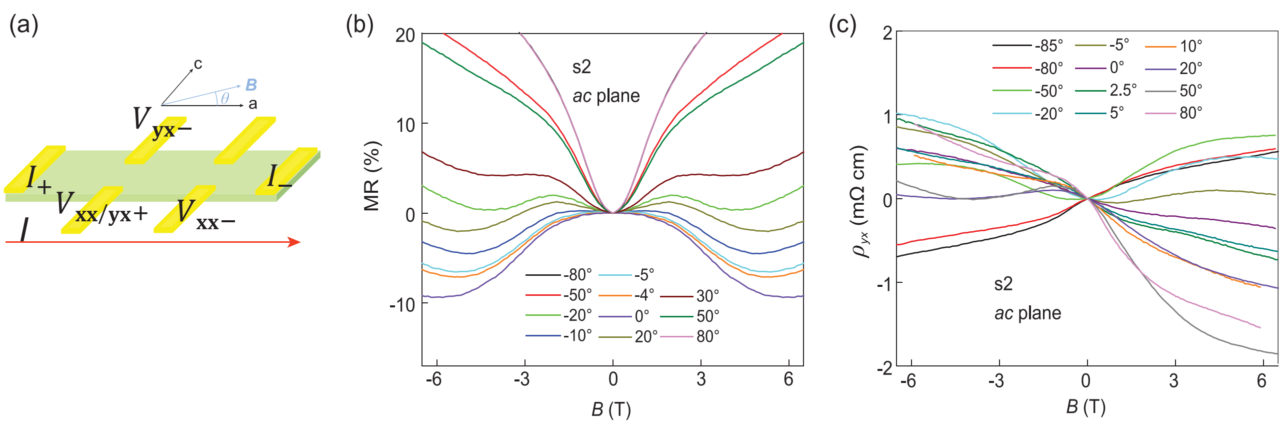

Figure 2. Angular dependence of magnetoresistance ratio and in-plane Hall resistivity in $ZrTe_5$ device s2. (a) Schematic structure for the angular-dependent magnetotransport measurements in *ac* plane. In-plane magnetic field is along a axis for $\theta = 0°$ ($B \parallel I$) and along c axis for $\theta = 90°$($B \perp I$). (b) MR behavior at selected angles. Negative LMR is detected in a large angular regime of $\pm 20°$ and reaches maximum at $\theta = 0°$ ($B \parallel I$). (c) In-plane Hall data after subtracting ρ_{xx} caused by slight electrodes misalignment through $\rho_{yx} = \rho_{yx}^{raw}(B) - \rho_{xx}(B) \cdot \frac{\rho_{yx}^{raw}(0)}{\rho_{xx}(0)}$. Both symmetric and antisymmetric contributions can be observed in ρ_{yx}.

$\rho_{yx}^{raw}(B) - \rho_{xx}(B) \cdot \frac{\rho_{yx}^{raw}(0)}{\rho_{xx}(0)}$. The raw Hall resistivity at selected angles can be found in Fig. S1. As shown in Fig. 2(c), the Hall traces exhibit both symmetric and antisymmetric components. More interestingly, nonzero Hall resistivity at $B \parallel I$ is clearly detected. This is forbidden in classical theory. The Hall resistivity should vanish at $\theta = 0°(B \parallel I)$ even considering the current model for planar Hall resistivity in Weyl semimetals [29,30].

To understand the detected in-plane Hall signals, we separately explore the symmetric and antisymmetric components in Hall traces. The symmetric component of the in-plane Hall resistivity is obtained by the symmetrization $\rho_{yx}^{s} = \frac{\rho_{yx}(+B)+\rho_{yx}(-B)}{2}$. Figure 3(a) displays the symmetric in-plane Hall resistivity $\rho_{yx}^{s}(B)$ at selected angles in s2. As the magnetic field is increased from 0 T to 6 T, the symmetric in-plane Hall resistivity grows and finally saturates at large magnetic field at most angles. More importantly, nonzero symmetric in-plane Hall resistivity at $B \parallel I$ ($\theta = 0°$) and $B \perp I$ ($\theta = 90°$) can be clearly observed. The temperature dependence of the symmetric in-plane Hall resistivity $\rho_{yx}^{s}(B)$ at $B \parallel I$ and $B \perp I$ is shown in Fig. 3(b) and (c), respectively. At a fixed magnetic field, the absolute values of $\rho_{yx}^{s}(B)$ at both $B \parallel I$ and $B \perp I$ decreases as temperature increases, and finally vanishes at about 200 K. To study how in-plane Hall behavior changes with the orientation between magnetic field and current, we detect the symmetric in-plane Hall resistivity as a function of θ at various magnetic fields. Figure 3(d) illustrates the symmetric in-plane Hall resistivity taken at various magnetic fields. The same symmetrization process is carried out to remove the contribution from the antisymmetric component. At $\theta = 0°(B \parallel I)$ and $\theta = 90°(B \perp I)$, the nonzero symmetric in-plane Hall resistivity can be clearly detected, which is in good consistence with the Hall results in Fig. 3a.

To obtain intrinsic antisymmetric in-plane Hall resistivity, we carried out angular-dependent magnetotransport measurements in *ac* plane of $ZrTe_5$ device s2 in a triple axes vector magnet. Figure 4(a) gives the antisymmetric in-plane Hall resistivity at selected angles taken at 1.1 K. The magnetic field lies in *ac* plane and is tilted away from the *a* axis ($\theta = 0°$). We define antisymmetric in-plane Hall resistivity as $\rho_{yx}^{as} = \frac{\rho_{yx}(+B)-\rho_{yx}(-B)}{2}$ to remove the contribution from the symmetric component. In low magnetic field region between −0.7 T and 0.7 T, linear behavior is observed at all angles. Nonzero antisymmetric in-plane Hall resistivity is detected at both $\theta = 0°(B \parallel I)$ and $\theta = 90°(B \perp I)$. We solely display the antisymmetric in-plane Hall resistivity near $B \parallel I$ and $B \perp I$ in Fig. 4(b) and (c) for clarity. As a comparison, Fig. S3 shows the antisymmetric in-plane Hall resistivity measured in Physical Property Measurement System (PPMS) after the same antisymmetrization process. Hall resistivity in the same magnetic field region from −0.7 T to 0.7 T is exhibited in Fig. S3(b), which is consistent with data in Fig. 3. Figure 4(d) and (e) shows temperature dependence of antisymmetric in-plane Hall resistivity ${\rho^{as}}_{yx}(B)$ at $B \parallel I$ and $B \perp I$. A linear $\rho_{yx}^{as}(B)$ behavior is clearly obtained. In low temperature regime, Hall resistivity at fixed magnetic fields slightly decreases with increasing temperature at both $B \parallel I$ and $B \perp I$.

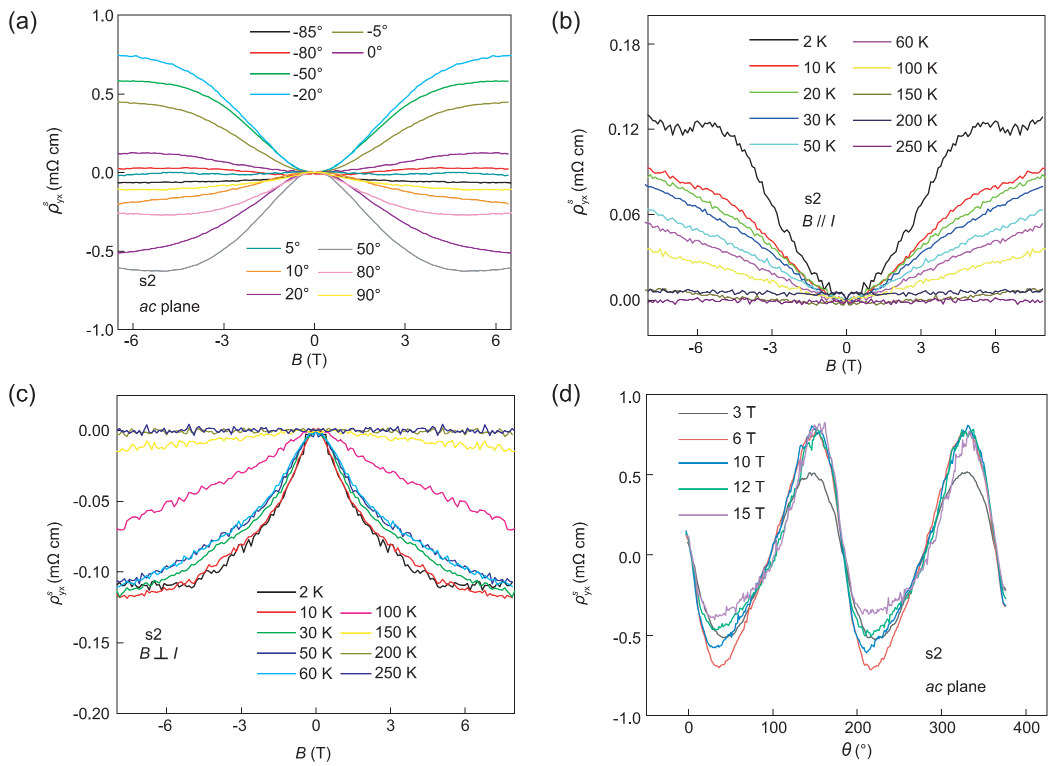

Figure 3. In-plane Hall signals detected in $ZrTe_5$ device s2 after symmetrization. Magnetic field lies in *ac* plane and is tilted away from the *a* axis ($\theta = 0°$). (a) Symmetric in-plane Hall resistivity vs. *B* at selected angles. Symmetric in-plane Hall resistivity grows as magnetic field increases, and saturates at high magnetic fields. (b, c) Symmetric in-plane Hall resistivity vs. *B* at $B \parallel I$ ($\theta = 0°$) and $B \perp I$ ($\theta = 90°$) at various temperatures. At a fixed magnetic field, the absolute values of symmetric in-plane Hall resistivity decreases as temperature increases, finally vanishing at about 200 K. (d) Symmetric in-plane Hall resistivity as a function of θ at different magnetic fields (T = 2 K) with $\rho^s_{yx} = \frac{\rho_{yx}(+B)+\rho_{yx}(-B)}{2}$. All curves indicate nonzero planar Hall resistivity at $B \parallel I$ ($\theta = 0°$) and $B \perp I$ ($\theta = 90°$).

To further confirm the detected nonzero Hall signals when in-plane magnetic field is parallel and perpendicular to the current, we carry out Hall measurements in other $ZrTe_5$ devices too. As shown in Fig. S5, similar nonzero Hall resistivity can be observed in device s1. Therefore, in topological $ZrTe_5$ devices, the Hall effect does exist when in-plane magnetic field is parallel and perpendicular to the current.

The nonzero Hall resistivity detected at $B \parallel I$ or $B \perp I$ is very unusual. In fact, this unconventional behavior can be understood as the PHE in a tilted topological semimetal. Previous studies on the PHE show that the conductivities depend quadratically on the magnetic field, and the Hall signal is zero when the electric field and the magnetic field are parallel and perpendicular [29,30]. However, we theoretically find that there are linear conductivities and nonzero Hall signal at $B \parallel I$ and $B \perp I$ in the PHE of tilted Weyl semimetals, where the anomalous velocity, the chiral chemical potential and the phase volume factor all play a part. $ZrTe_5$ is considered as a topological semimetal in magnetic field [38]. Specifically, we investigate a low energy effective model [37] based on previous density functional theory calculation [35] and find that magnetic field drives $ZrTe_5$ into a tilted Weyl semimetal phase with a pair of Weyl points. (See the Supplementary Information for details.) This is not surprising, since tilt is common among Weyl semimetals, as Weyl points are typically low-symmetry points [42,43]. We performed a semiclassical calculation on the conductivities of a tilted Weyl semimetal and compare the theoretical findings with the experimental results. (See the Supplementary Information for details.) As shown in Fig. 4(f), the black circle data points are the angular dependence of observed in-plane Hall conductivity detected in a vector magnet at 1.1 K and 1 T. The in-plane Hall conductivity σ_{yx} is calculated by $\sigma_{yx} = \frac{-\rho_{yx}}{(\rho^2_{yx}+\rho^2_{xx})}$, here, ρ_{yx} is the in-plane Hall resistivity after subtracting ρ_{xx} caused by slight electrodes misalignment through $\rho_{yx} = \rho^{raw}_{yx}(B) - \rho_{xx}(B) \cdot \frac{\rho^{raw}_{yx}(0)}{\rho_{xx}(0)}$. The red theoretical fitting curve with a

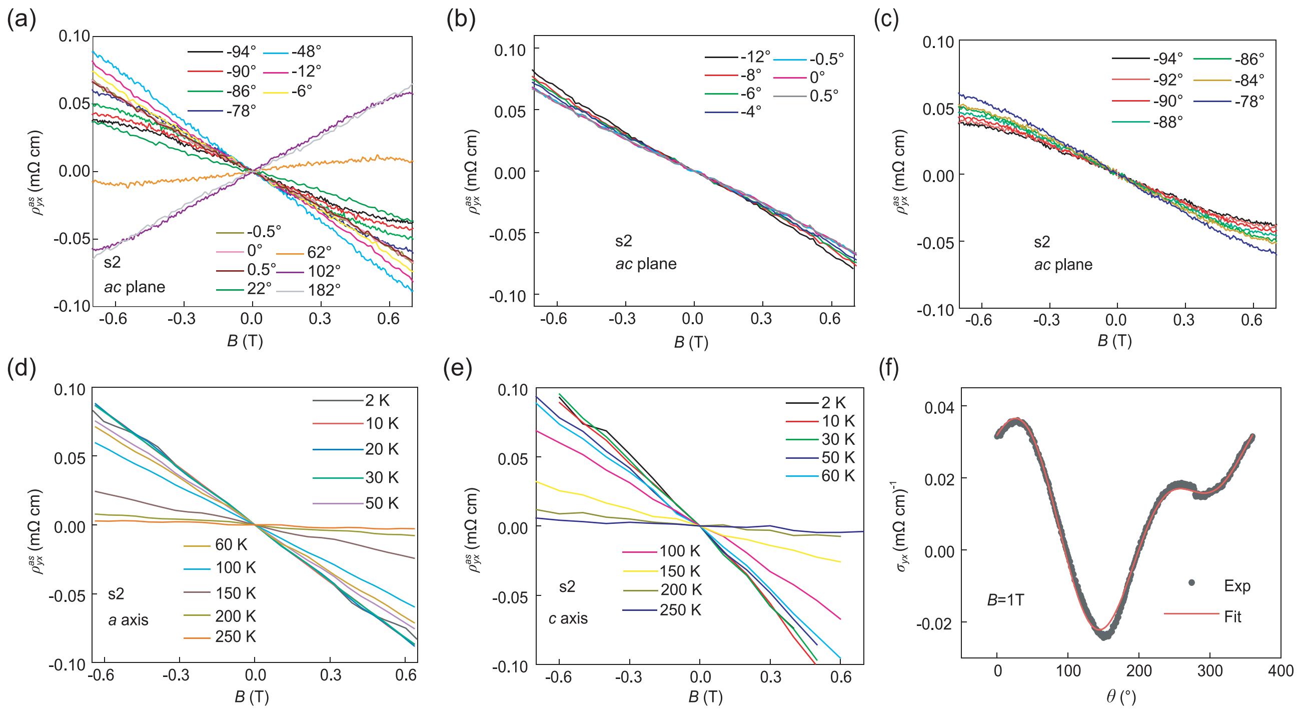

Figure 4. In-plane Hall resistivity detected in $ZrTe_5$ device s2 after antisymmetrization and theoretical fitting of the observed in-plane Hall conductivity. Magnetic field lies in *ac* plane and is tilted away from the *a* axis ($\theta = 0^\circ$). (a) Antisymmetric in-plane Hall resistivity vs. B at selected angles. Linear behavior at low magnetic fields can be observed. (b, c) Antisymmetric in-plane Hall resistivity vs. B around $B \parallel I$ ($\theta = 0^\circ$) and $B \perp I$ ($\theta = 90^\circ$). Antisymmetric in-plane Hall signal is also apparent at both $B \parallel I$ ($\theta = 0^\circ$) and $B \perp I$ ($\theta = 90^\circ$). (d, e) Antisymmetric in-plane Hall resistivity versus B at $B \parallel I$ ($\theta = 0^\circ$) and $B \perp I$ ($\theta = 90^\circ$) at various temperatures. All Hall traces show linear behavior in low field region. (f) Theoretical fitting (red curve) of the in-plane Hall conductivity after excluding ρ_{xx} caused by slight electrodes misalignment.

set of reasonable parameters (listed in Supplementary Information) is well consistent with the experimental data [39].

The Dirac cones in $ZrTe_5$ may open a small gap Δ of the order several meV in *ab initio* calculations [26] considering the precise value of the spin orbital coupling strength. Nevertheless, in our samples $E_F >> \Delta$ is satisfied, indicating that the gap has little impact on the Berry curvature and the Fermi velocity at the Fermi surface. Therefore, our theoretical conclusion stands even considering a small gap in $ZrTe_5$.

CONCLUSION

In summary, we fabricated and measured $ZrTe_5$ devices with standard Hall bar structure. The detected Hall signals exhibit both symmetric and antisymmetric behavior when the magnetic field is in *ac* plane. After removing the contributions from LMR caused by slight misalignment of electrodes and projection of normal Hall with $B \parallel b$ axis, nonzero in-plane Hall resistivity is clearly obtained when in-plane magnetic field is parallel and perpendicular to the current, which is unprecedented in previous theoretical and experimental studies. Theoretical calculation suggests that the unconventional behavior of the Hall conductivity can be understood within the semiclassical transport of the tilted Weyl semimetals, where the chiral chemical potential, the Berry curvature-induced anomalous velocity and the phase space volume correction all take part. Our discovery of nonzero in-plane Hall signals at $B \parallel I$ and $B \perp I$ not only adds a new member to the Hall effect family but also paves a new way to explore Berry phase and Berry curvature in topological materials.

METHODS

Fabrication of $ZrTe_5$ flake devices

The $ZrTe_5$ bulk crystals were grown as described in reference [38]. $ZrTe_5$ flakes supported by 300 nm-thick SiO_2/Si substrates were mechanically exfoliated from high quality single crystals with scotch tape. The detailed fabrication process of electrodes is described below.

(i) Standard Electron beam lithography in a FEI Helios NanoLab 600i DualBeam System to define electrodes after spin-coating PMMA resist;

(ii) Develop resist in an IPA: MIBK (3:1 by weight) mixture;
(iii) Deposit Pd (6.5 nm)/Au (300 nm) in a LJUHV E-400 L E-Beam Evaporator after Ar plasma cleaning;
(iv) Remove PMMA layers by standard lift-off process.

Transport measurements

Electrical transport measurements are conducted in a 16T-Physical Property Measurement System (PPMS-16T) from Quantum Design at 2 K and a Leiden dilution refrigerator (CF450) with a triple axes vector magnet at 1.1 K.

SUPPLEMENTARY DATA

Supplementary data are available at *NSR* online.

FUNDING

This work was supported by the National Key Research and Development Program of China (2018YFA0305604 and 2017YFA0303300), the National Natural Science Foundation of China (11888101 and 11774008), the Strategic Priority Research Program of Chinese Academy of Sciences (XDB28000000), and the Beijing Natural Science Foundation (Z180010). Work at ORNL was supported by the U.S. Department of Energy, Office of Science, Basic Energy Sciences, Materials Sciences and Engineering Division.

AUTHOR CONTRIBUTIONS

J.W. conceived the research and supervised the experiments. J.G., Y. Liu, H.W., Y. Li, J.L. and T. L. performed the electrical transport measurements and analyzed the data. D. Ma, H.L. and X.C.X developed the theoretical model. J.Y. and D. Mandrus grew the bulk crystals. J.G. and Y. Li. fabricated the devices. All authors offered discussion or revisions on the manuscript.

Conflict of interest statement. None declared.

REFERENCES

1. Berry MV. Quantal phase factors accompanying adiabatic changes. *Proc R Soc London Ser A* 1984; **392**: 45–7.
2. Adams EN and Blount EI. Energy bands in the presence of an external force field II. Anomalous velocities. *J Phys Chem Solids* 1959; **10**: 286–303.
3. Blount EI. *Solid State Physics*. San Diego: Academic Press, 1962.
4. Chang MC and Niu Q. Berry curvature, orbital moment, and effective quantum theory of electrons in electromagnetic fields. *J Phys Condens Matter* 2008; **20**: 193202.
5. Chang MC and Niu Q. Berry phase, hyperorbits, and the Hofstadter spectrum. *Phys Rev Lett* 1995; **75**: 1348–51.
6. Gradhand M, Fedorov DV and Pientka F *et al.* First-principle calculations of the Berry curvature of Bloch states for charge and spin transport of electrons. *J Phys Condens Matter* 2012; **24**: 213202.
7. Fläschner N, Rem BS and Tarnowski M *et al.* Experimental reconstruction of the Berry curvature in a Floquet Bloch band. *Science* 2016; **352**: 1091–4.
8. Fang Z, Nagaosa N and Takahashi KS *et al.* The anomalous Hall effect and magnetic monopoles in momentum space. *Science* 2003; **302**: 92–5.
9. Sundaram G and Niu Q. Wave-packet dynamics in slowly perturbed crystals: gradient corrections and Berry-phase effects. *Phys Rev B* 1999; **59**: 14915–25.
10. Haldane FDM. Berry curvature on the Fermi surface: anomalous Hall effect as a topological Fermi-liquid property. *Phys Rev Lett* 2004; **93**: 206602.
11. Liu CX, Qi XL and Dai X *et al.* Quantum anomalous Hall effect in $Hg_{1-y}Mn_{1-y}Te$ quantum wells. *Phys Rev Lett* 2008; **101**: 146802.
12. Son DT and Yamamoto N. Berry curvature, triangle anomalies, and the chiral magnetic effect in Fermi liquids. *Phys Rev Lett* 2012; **109**: 181602.
13. Nagaosa N, Sinova J and Onoda S *et al.* Anomalous Hall effect. *Rev Mod Phys* 2010; **82**: 1539–92.
14. Yu R, Zhang W and Zhang HJ *et al.* Quantized anomalous Hall effect in magnetic topological insulators. *Science* 2010; **329**: 61–4.
15. Onoda M and Nagaosa N. Quantized anomalous Hall effect in two dimensional ferromagnets: quantum Hall effect in metals. *Phys Rev Lett* 2003; **90**: 206601.
16. Taguchi Y. Spin chirality, Berry phase, and anomalous Hall effect in a frustrated ferromagnet. *Science* 2001; **291**: 2573–6.
17. Jungwirth T, Niu Q and MacDonald AH. Anomalous Hall effect in ferromagnetic semiconductors. *Phys Rev Lett* 2002; **88**: 207208.
18. Yao Y, Kleinman L and MacDonald AH *et al.* First principles calculation of anomalous Hall conductivity in ferromagnetic bcc Fe. *Phys Rev Lett* 2004; **92**: 037204.
19. Wang J, Li HD and Chang CZ *et al.* Anomalous anisotropic magnetoresistance in topological insulator films. *Nano Res* 2012; **5**: 739–46.
20. Dai X, Du ZZ and Lu HZ. Negative magnetoresistance without chiral anomaly in topological insulators. *Phys Rev Lett* 2017; **119**: 166601.
21. Du ZZ, Wang CM and Lu HZ *et al.* Band signatures for strong nonlinear Hall effect in bilayer WTe_2. *Phys Rev Lett* 2018; **121**: 266601.
22. Du ZZ, Wang CM and Li S *et al.* Disorder-induced nonlinear Hall effect with time-reversal symmetry. *Nat Commun* 2019; **10**: 3047–52.
23. Xiao D, Shi J and Niu Q. Berry phase correction to electron density of states in solids. *Phys Rev Lett* 2005; **95**: 137204.
24. Wan X, Turner AM and Vishwanath A *et al.* Topological semimetal and Fermi-arc surface states in the electronic structure of pyrochlore iridates. *Phys Rev B* 2011; **83**: 205101.

25. Xu G, Weng H and Wang Z *et al.* Chern semimetal and the quantized anomalous Hall effect in $HgCr_2Se_4$. *Phys Rev Lett* 2011; **107**: 186806.
26. Weng H, Fang C and Fang Z *et al.* Weyl semimetal phase in noncentrosymmetric transition-metal monophosphides. *Phys Rev X* 2015; **5**: 011029.
27. Hosur P and Qi X. Recent developments in transport phenomena in Weyl semimetals. *C R Phys* 2013; **14**: 857–70.
28. Son DT and Spivak BZ. Chiral anomaly and classical negative magnetoresistance of Weyl metals. *Phys Rev B* 2013; **88**: 104412.
29. Burkov AA. Giant planar Hall effect in topological metals. *Phys Rev B* 2017; **96**: 041110.
30. Nandy S, Sharma G and Taraphder A *et al.* Chiral anomaly as the origin of the planar Hall effect in Weyl semimetals. *Phys Rev Lett* 2017; **119**: 176804.
31. Li P, Zhang CH and Zhang JW *et al.* Giant planar Hall effect in the Dirac semimetal $ZrTe_{5-\delta}$. *Phys Rev B* 2018; **98**: 121108.
32. Liang DD, Wang YJ and Zhen WL *et al.* Origin of planar Hall effect in type-II Weyl semimetal $MoTe_2$. *AIP Adv* 2019; **9**: 055015.
33. Wu M, Zheng GL and Chu WW *et al.* Probing the chiral anomaly by planar Hall effect in Dirac semimetal Cd_3As_2 nanoplates. *Phys Rev B* 2018; **98**: 161110.
34. Shama, Gopal RK and Singh Y. Observation of planar Hall effect in the magnetic Weyl semimetal $Co_3Sn_2S_2$. arXiv: 1810.04867.
35. Weng H, Dai X and Fang Z. Transition-metal pentatelluride $ZrTe_5$ and $HfTe_5$: a paradigm for large-gap quantum spin Hall insulators. *Phys Rev X* 2014; **4**: 011002.
36. Li Q, Kharzeev DE and Zhang C *et al.* Chiral magnetic effect in $ZrTe_5$. *Nat Phys* 2016; **12**: 550–4.
37. Chen RY, Chen ZG and Song XY *et al.* Magnetoinfrared spectroscopy of Landau levels and Zeeman splitting of three-dimensional massless Dirac fermions in $ZrTe_5$. *Phys Rev Lett* 2015; **115**: 176404.
38. Wang H, Liu HW and Li YN *et al.* Discovery of log-periodic oscillations in ultraquantum topological materials. *Sci Adv* 2018; **4**: eaau5096.
39. Liu YW, Yuan X and Zhang C *et al.* Zeeman splitting and dynamical mass generation in Dirac semimetal $ZrTe_5$. *Nat Commun* 2016; **7**: 12516.
40. Liang T, Lin JJ and Gibson Q *et al.* Anomalous Hall effect in $ZrTe_5$. *Nat Phys* 2018; **14**: 451–5.
41. Niu JJ, Wang JY and He ZJ *et al.* Electrical transport in nanothick $ZrTe_5$ sheets: from three to two dimensions. *Phys Rev B* 2017; **95**: 035420.
42. Soluyanov AA, Gresch D and Wang ZJ *et al.* Type-II Weyl semimetals. *Nature* 2015; **527**: 495–8.
43. Trescher M, Sbierski B and Brouwer PW *et al.* Quantum transport in Dirac materials: signatures of tilted and anisotropic Dirac and Weyl cones. *Phys Rev B* 2015; **91**: 115135.